Alloyed Ni-Fe nanoparticles as catalysts for NH3 decomposition

Simonsen, Søren Bredmose; Chakraborty, Debasish; Chorkendorff, Ib; Dahl, Søren

Published in:
Applied Catalysis A: General

Link to article, DOI:
10.1016/j.apcata.2012.08.045

Publication date:
2012

Document Version
Peer reviewed version

Alloyed Ni-Fe nanoparticles as catalysts for NH_3 decomposition

Søren Bredmose Simonsen[a], Debasish Chakraborty[b], Ib Chorkendorff[a], Søren Dahl[a]

[a]CINF, Department of Physics, Technical University of Denmark, Fysikvej, building 307, DK-2800 Lyngby, Denmark
[b]Amminex A/S, Gladsaxevej 363, DK-2860 Søborg, Denmark

Corresponding author: Søren Bredmose Simonsen, sobrs@dtu.dk, phone: + 45 4677 5800

Abstract

A rational design approach was used to develop an alloyed Ni-Fe/Al_2O_3 catalyst for decomposition of ammonia. The dependence of the catalytic activity is tested as a function of the Ni-to-Fe ratio, the type of Ni-Fe alloy phase, the metal loading and the type of oxide support. In the tests with high temperatures and a low NH_3-to-H_2 ratio, the catalytic activity of the best Ni-Fe/Al_2O_3 catalyst was found to be comparable or even better to that of a more expensive Ru-based catalyst. Small Ni-Fe nanoparticle sizes are crucial for an optimal overall NH_3 conversion because of a structural effect favoring the smallest particles in terms of catalytic activity per active site. Compared with SiO_2, ZrO_2 and TiO_2, the support materials Al_2O_3 or Mg-Al-spinel give the highest performance in the high temperature range.

Keywords
Catalysis, NH_3 decomposition, nickel-iron alloy, hydrogen storage, hydrogen production, fuel cell

1 Introduction

Hydrogen can be used as an environmentally clean energy carrier to power for example fuel cells and internal combustion engines [1]. However, serious challenges related to hydrogen as energy vector, such as the development of safe infrastructures for hydrogen storage and distribution must be addressed. In this relation, NH_3 has a number of favorable attributes, the primary one being its high capacity for H_2 storage [2,3], and that NH_3 can be safely stored in salts such as $MgCl_2$ with a high density of H_2 compared to liquid H_2 [4]. Ammonia is the second largest chemical in terms of production volume. More than 130 million tons of NH_3 is produced each year, bulk of which is used as fertilizer and the infrastructure for transport of NH_3 in large scale already exists [2].

To be able to use H_2, stored in NH_3, it is necessary to decompose the NH_3 into H_2 and N_2, and this is done most efficiently by using a catalyst [5]. The most active catalysts for NH_3 decomposition are based on noble metals like Ru, Rh, Pt, Ir as well as the non-noble metals Ni and Fe [6-13]. The catalytic performance of these metals is typically enhanced by distributing the metals on a high surface area support material, such as an oxide [6,7,10-13] or carbon-based material [6-9,12,13]. The catalytic activity may further be enhanced by the use of promoters such as K, Na, Li, Ce, Ba, La, Ca, Cs [6,7,9-13].

Theoretical models, describing the activity of catalysts for ammonia synthesis as a function of the N_2 dissociative chemisorption energy for transition metals in so-called volcano plots [14], have been shown to be applicable to the ammonia decomposition reaction as well [15]. The volcano plot presents Ru near the top of the curve, as indicated by fig. 1 which is reprinted from reference [15]. Ni and Fe are less catalytically active and are found to the right and left side, respectively, of Ru in the volcano plot (fig. 1). The shape of the volcano plot implies that there is an optimum for the adsorption energy, which reflects the compromise that a good catalyst should be able to activate the reactants, but not bind the reaction intermediates and products too hard. Previous studies have used a rational approach to design catalysts, where the idea was to combine metals with high and low binding energies to obtain an alloy with optimal interaction strength, resulting in a high catalytic activity [16]. For the ammonia synthesis reaction a Co-Mo-based catalyst with a relatively high activity was designed by using this approach [16]. Similarly, a highly active ammonia decomposition catalyst could possibly be developed by alloying metals from both sides of the peak of the volcano curve (fig. 1), e.g. Ni and Fe. A few alloys have already been developed as catalysts for NH_3 decomposition, for example related to NO_x emissions in fossil-fuel fired power plants [17], but also related to the conversion of NH_3 into H_2 [18-20]. These are, however, only described in patents from which the exact alloy composition and the catalytic performance is not fully transparent.

A factor that complicates the approach of finding an alloy with an optimal peak position in the volcano plot, is that the peak position depends on the reaction conditions [5,15]: For high NH_3-to-H_2 ratios (e.g. 99% NH_3) the peak position is between the nitrogen binding energies for Ru and Ni, while a decrease in the NH_3-to-H_2 ratio results in a movement of the peak to the left towards the nitrogen binding energy for Fe (fig. 1). This is also the reason why the optimal catalyst for ammonia decomposition is not identical to the optimal catalyst for ammonia synthesis [15].

A different and significant effect of a decreasing NH_3-to-H_2 ratio is the slowing down of the decomposition reaction resulting from an established equilibrium between adsorbed N atoms, gas-phase NH_3 and gas-phase H_2 [8]. This effect is a challenge if one aims for an end product with close to 100% H_2 and only traces of NH_3, for example in relation to PEM fuel cell applications where NH_3 poisons the fuel cell [3].

In the present study we apply the rational design approach based on the volcano curve to develop an alloyed catalyst for decomposition of NH_3. We focus on Ni and Fe, since these are relatively inexpensive and abundant. We test the dependence of the activity of the alloyed phase as a function of several parameters such as the Ni-to-Fe ratio, type of Ni-Fe alloy phase, metal loading and type of the oxide support. To describe the influence of the gas environment on the catalytic performance, all tests were performed both at a high and a low NH_3-to-H_2 ratio in the feed gas. In agreement with the theoretical considerations it is found that the alloyed Ni-Fe/Al_2O_3 catalyst has a high activity compared to Ni/Al_2O_3 or Fe/Al_2O_3 catalysts in the hydrogen rich gas environment. The catalytic activity per active site is found to increase with decreasing average particle size.

2 Experimental

2.1 Catalyst preparation

The catalysts were prepared by incipient wetness impregnation of spherical γ-Al_2O_3 pellets with a diameter of 1 mm (Sasol Germany GmbH) with a aqueous solution of Ni and Fe nitrates. The samples were dried at RT for at least 48 h. Further drying and calcination was carried out in air at 100°C for 10 h and at 450°C for 4 h in a tube furnace. Three different types of catalysts were prepared in this way: Ni/Al_2O_3, Fe/Al_2O_3 and alloyed Ni-Fe/Al_2O_3 with a desired metal loading of 10 wt.% for all three types. For the alloyed Ni-Fe/Al_2O_3 catalyst, the desired Ni-to-Fe ratio was varied from 5 wt.% to 80 wt.% Ni. To determine the effect of metal loading, a series of catalysts were prepared with metal loading varying from 5% to 23% and a constant Ni concentration in the metal phase of 20 wt.%. To achieve metal loadings above 10%, it was necessary to impregnate the pellets repeatedly. For comparison with Al_2O_3, the following oxides were also impregnated: Mg-Al spinel (28% MgO) powder (Sasol Germany GmbH), SiO_2 extrudates (Saint-Gobain Norpro), ZrO_2 pellets (Saint-Gobain Norpro) and TiO_2 pellets (Saint-Gobain Norpro).

To compare with a different preparation method, an alloyed Ni-Fe/Al_2O_3 catalyst with 10 wt.% metal loading and 20 wt.% Ni in the active phase was prepared by coprecipitation in the following way: Ni, Fe and Al nitrates in the appropriate molar ratios were dissolved in H_2O. The total concentration of nitrate was 0.4 M. Over a period of ca. 1 h, the nitrate solution was mixed with an 0.4 M ammonium carbonate solution by dripping them into a glass beaker containing H_2O under vigorous stirring. Approximately identical dripping rates were obtained for both solutions by maintaining the pH at 6 ±1. The precipitate was aged for 1 h in the mother liquor. After ageing, the sample was suction filtered and washed. The obtained solid was dried in air at 110°C overnight. The samples were calcined at 500°C for 5 h.

2.3 Catalytic testing

The catalyst testing was carried out in a tubular continuous flow quartz reactor with an inner diameter of 4 mm. When comparing the catalytic activity of different catalysts supported on γ-Al_2O_3, whole catalyst pellets were used. When comparing the catalytic activity for different support types or for different synthesis methods, the samples were crushed and sieved to a grain size of ca. 200 – 400 µm to exclude possible differences resulting from variations of pellets sizes and shapes. The catalyst bed was composed of 50 mg catalyst + 50 mg γ-Al_2O_3 as inert.

Immediately before testing, the catalysts were reduced in a flow of 100 ml/min of H_2 by ramping up the temperature by 10°C/min to 800°C and maintaining this temperature for 1 h.

To simulate the difference in NH_3-to-H_2 ratio in the first and very last part of a plug flow reactor decomposing pure ammonia, the activity tests were performed at a gas pressure of 1 bar and a flow of 200 ml/min in two different gas environments; test A: 1000 ppm NH_3 balanced by a 50%-50% mixture of Ar and He (simulating the first part of the bed with a high NH_3-to-H_2 ratio) and test B: 1000 ppm NH_3 balanced by a 50%-50% mixture of Ar and H_2 (simulating the very last part of the bed with a low NH_3-to-H_2 ratio). For both gas environments GHSV ≈ 80.000 1/h and 95.000 1/h for beds with whole catalyst spheres and smaller grains, respectively.

The product analysis was performed with an online quadropole mass spectrometer (Pfeiffer OmniStar GSD320 O1 equipped with an Y-Ir filament) calibrated against different ratios of NH_3 and Ar. The activity was measured for the temperatures 400ºC, 500ºC, 600ºC, 700ºC and 800ºC after holding each temperature for at least 30 min. The conversion of NH_3 is presented with an error of 2 percentage points, estimated as the measured mean difference in NH_3 conversion for two different Ni-Fe/Al_2O_3 catalyst batches.

2.3 Characterization

The BET surface areas of the support materials were measured by N_2 adsorption at -196°C by using a Micromeritics Gemini 1490. The measurements were carried out on approximately 0.2 g of the support oxides before and after reduction for 5 h in a flow of 100 ml/min of H_2 at 800°C. Prior to the BET measurements the samples were dried overnight at 150°C in a flow of N_2 by using a Micromeritics Flow Prep 060. An error of 3% was estimated for the determined surface areas from the difference of two measurements of the fresh Al_2O_3.

TEM was performed with a Tecnai T20 G2 (FEI Company) equipped with a thermionic LaB6 electron source and operated at a primary electron energy of 200 keV. TEM images were acquired by using a bottom-mounted 2k x 2k CCD camera (Gatan 894 2K UltraScan 1000). Except for high resolution images, a 40 µm objective aperture was used to enhance the contrast. The metal contents were determined by energy-dispersive spectroscopy (EDS) by using an Oxford Instruments 80 mm^2 X-Max SDD. The catalyst samples were prepared for TEM imaging and analysis by grinding in a mortar into a fine powder and adding ethanol. Drops of the liquid dispersion were then added on lacey carbon-coated Cu grids. From the TEM images, Ni-Fe nanoparticle sizes were measured manually by outlining the particles and calculating the mean diameter of each particle from the outlined area by assuming a circular perimeter. The estimated measuring error is a systematic error of 10 % of the particle diameters due to calibration of the TEM and an estimated random error of 0.8 nm due to the manual image analysis. The bin sizes in the presented particles size distributions were optimized by the formula given in reference [21].

Ex situ and in situ X-ray diffraction (XRD) measurements were performed on a PANalytical X'Pert PRO diffractometer using CuKα1 radiation. The catalyst samples were prepared for XRD analysis by grinding in a mortar into a fine powder. Scans were recorded in the range of 2θ = 10–110°. For in situ XRD, fresh calcined catalyst powder samples were mounted in an Anton Paar XRK hot stage provided with gas inlet and outlet lines. Initially, a scan was recorded in air at RT. In a flow = 20 ml/min of 1 bar H_2, the temperature was then ramped at a rate of 10°C/min from RT to 600°C, 700°C and 800°C. At each temperature scans were recorded in the range of 2θ = 41 – 55° over 45 min. For all scans, the temperatures were remained stable during scanning. At T = 800°C, three scans were recorded, so that the total reduction time at this temperature was ca. 2 h and 15 min. Finally, the temperature was ramped down in H_2 with a rate of ca. 20°C/min. and a scan was recorded at RT in H_2.

3 Results and discussion

To determine the catalytic activity, a series of Ni-Fe/Al_2O_3 catalysts with varying Ni concentration in the active phase were tested. Fig. 2 presents the conversion of NH_3 for these catalysts as a function of reaction temperature for (a) test A and (b) test B.

3.1 The pure metals

For both test A and B, it can be seen that the Ni/Al_2O_3 catalyst (fig. 2a-b, black x) has a higher catalytic activity than Fe/Al_2O_3 (fig. 2a-b, grey square). For comparison with a noble-metal based catalyst, the test result of a commercial Ru/Al_2O_3 (same type of Al_2O_3 support pellets) catalyst is also presented (fig. 2a-b, open square). The comparison gives the same order of catalytic activity as found in the majority of other studies (Ru > Ni > Fe) [7-9,22,23], but a higher activity of Fe over Ni has also been observed [12]. It should be emphasized that the metal loading of the Ru/Al_2O_3 catalyst is only 2 wt.% while that of the other catalysts in fig. 2 is 10 wt.%. From fig. 2a-b it can be seen that the conversion is much closer to the calculated thermodynamic equilibrium (fig. 2a-b, dashed line) for test A (fig. 2a) than for test B (fig. 2b). This illustrates the inhibitory effect of gas phase H_2 to the decomposition reaction of NH_3 and highlights the challenge of getting very close to the equilibrium in a realistic NH_3 cracking reactor.

3.2 The Ni-to-Fe ratio

Now focusing on the alloyed Ni-Fe/Al_2O_3 catalysts presented in fig. 2, it can be seen that all of these catalysts have a higher performance than the pure Fe/Al_2O_3 catalyst in both tests. This effect could either be explained by the formation of an alloy with a more optimal nitrogen binding energy according to the volcano curve, or simply by the addition of a pure Ni phase which has a higher catalytic activity than pure Fe according to fig. 2a-b. A comparison of the alloyed Ni-Fe/Al_2O_3 catalysts with the Ni/Al_2O_3 catalyst indicates influence of an alloyed phase: while the Ni/Al_2O_3 catalyst has the highest activity in test A for all reaction temperatures, the catalytic activity in test B has the following order: 20-50 wt.% Ni > 80-100 wt.% Ni > 0-10 wt.% Ni. The trends are perhaps more clearly illustrated by fig. 2c, where the NH_3 conversions are plotted directly as a function of the Ni concentration. The results agree well with the previously determined shift of the peak position in the volcano curve from the nitrogen binding energy of Ni towards that of Fe when the NH_3-to-H_2 ratio decreases [15].

Fig. 2 therefore shows that an alloyed Ni-Fe/Al_2O_3 with 20-50 wt.% in the active phase has a better performance than a pure Ni/Al_2O_3 towards NH_3 decomposition when the gas composition is close to equilibrium. In the hydrogen rich environment, the performance of the best alloyed Ni-Fe/Al_2O_3 with 10 wt.% metal loading are however not as good as that of the Ru/Al_2O_3 catalyst.

3.3 The active phase

To determine the catalytically active phase, ex situ and in situ XRD was performed on the Ni-Fe/Al_2O_3 catalysts with 20 wt.% Ni in the active phase and 10 wt.% metal loading. Fig. 3a presents ex situ XRD patterns of the Ni-Fe/Al_2O_3 catalyst before reduction, after reduction for 1 h, after reduction for 6 h and of the Al_2O_3 support as a reference. All visible peaks of the Ni-Fe/Al_2O_3 catalyst before reduction are also present in the patterns of the Al_2O_3 support (fig. 3a), while

additional peaks appear after the reduction process (fig. 3a). Before the reduction, the Ni and Fe are therefore most probably highly distributed as Ni-oxide and Fe-oxide species, and the formation of new crystalline phases takes place during the reduction. The additional peaks in the patterns of the reduced Ni-Fe/Al_2O_3 catalysts have peaks positioned close to reference lines for the Ni-Fe alloy phases, Kamacite (fig. 3a, black vertical lines) and Taenite (fig. 3a, grey vertical lines). It should however be noted that the reference lines for Kamacite are situated close to the reference lines for pure Fe (not shown), and fig. 3a could therefore also indicate the presence of pure Fe in the reduced samples. The patterns of the two reduced catalysts are not identical, but show a significant difference of the intensity of the additional peaks. Specifically, the dominating additional peaks in the patterns of the catalyst that is reduced for 1 h fits with the reference lines for Kamacite, while the dominating additional peaks in patterns of the catalyst that is reduced for 6 h fits with the reference lines for Taenite (fig. 3a).

To study the phase transformation during reduction as indicated by fig. 3a, in situ XRD patterns were recorded of the Ni-Fe/Al_2O_3 catalyst during a reduction process. Fig. 3b presents the in situ XRD patterns I to VII recorded as a function of time and temperature at 2theta = 41° - 55°, covering just the main Ni-Fe alloy reference lines. The peaks that develop over time are positioned close to the reference lines for the Ni-Fe alloy phases, first close to the reference line for Kamacite (fig. 3b, black vertical line) and, for temperatures above 600°C, also close to the reference lines for Taenite (fig. 3b, grey vertical lines). The shifts in peak positions between the patterns recorded at the elevated temperatures and RT are due to thermal expansion of the sample holder. The observations from fig. 3b are consistent with the observations from fig. 3a, that the Kamacite phase appear after the relatively short reduction time of 1 h, while at 800°C the Taenite phase grows with the extended reduction time. The observations are also consistent with the phase diagram for Ni-Fe alloys, according to which Taenite dominates at temperatures above ca. 600°C, while both phases coexists a lower temperatures [24]. Fig. 3a-b therefore show that both Kamacite and Taenite forms during reduction, but the Kamacite phase over time transforms into Taenite. The reduction time is therefore an important parameter for obtaining the specific alloy phase.

For catalysts operating at temperatures above 600°C, fig. 3 suggests that the Taenite eventually will be the dominating phase. For catalysts operating at lower temperatures, both alloyed phases are more stable and the phase with the highest catalytic activity can be obtained by controlling the reduction time. Since two different Ni-Fe alloy phases can occur in the Ni-Fe/Al_2O_3 catalyst, it is important to determine the catalytic activity of each phase. Fig. 4a-b presents the catalytic activity of two Ni-Fe/Al_2O_3 catalysts as a function of temperature, where one of the catalysts was reduced for 1 h (grey) and the other was reduced for 6 h (black). The two catalysts therefore represent the catalytic activity towards NH_3 decomposition of Kamacite (grey) and Taenite (black), respectively. According to fig. 4 the catalytic activity is similar for both alloy phases, although Taenite may be slightly more active in test A, while Kamacite is slightly more active in test B. It should be noticed, that Kamacite has a relatively low maximum concentration of Ni (up to ca. 10 wt.% Ni) while Taenite eventually will obtain the nominal Ni concentration (in this case 20 wt.% Ni) according to the Ni-Fe alloy phase diagram [24]. Since the peak of the volcano curve shifts towards the nitrogen binding energy of Fe for decreasing NH_3-to-H_2 ratios [15], it could therefore have been expected

that the Fe-rich Kamacite would perform relatively better in test B, compared to Taenite, and vice versa. It should, however, be noticed that the catalysts referred to by fig. 4 does not represent the pure alloy phases, but mixed phases where either Kamacite or Taenite dominates, which may complicate the comparison with the trends of the volcano curve.

3.4 Metal loading and particle size

Fig. 5a-b presents the conversion of NH_3 for the catalysts with varying metal loading. For test B (fig. 5b), the observed slight increase in conversion with increasing metal loading is approximately within the measurement error of ca. 2% points, but for test A (fig. 5a), increasing NH_3 conversions are observed for increasing metal loadings. The effect, however, appears to be small, which could suggest a relative loss of active surface area due to increasing particle sizes for increasing loadings and possibly also a structural effect related to the nanoparticle sizes.

To investigate possible differences in the particle sizes, TEM images were acquired of the Ni-Fe/Al_2O_3 catalysts with different metal loadings. As an example fig. 6a presents a representative TEM image of the Ni-Fe/Al_2O_3 with 10% metal loading. In the TEM image, a large irregular feature can be observed on a lighter background. The large irregular area is attributed to the Al_2O_3 support material, and the brighter background corresponds to the vacuum in the microscope (fig. 6a). In the lower corners of fig. 6a a light grey feature can be observed, which corresponds to lacey carbon on the TEM grid. Smaller, approximately circular, darker areas are observed within the Al_2O_3, and these are attributed to the Ni-Fe phase. Indeed, high resolution TEM images of the small dark areas show lattice fringes with distances of 2.0 - 2.1 Å, which within the 10% calibration error of the TEM, corresponds to the reference lattice distances for Ni ([111]: 2.0 Å), Fe ([110]: 2.0) and Ni-Fe alloys; Kamacite ([111]: 2.0 Å) and Taenite ([111]: 2.1 Å). Examples of HRTEM images are given in fig. 7. Here lattice spacings for the nanoparticles and the support materials can be seen for two difference catalysts, either directly in the TEM images (fig. 7a,d) or as spots in reciprocal space represented by Fourier transforms (Fig. 7b,e). In addition, inverse Fourier transforms of masked areas of the Fourier transforms indicate the areas dominated with 2.0-2.1 Å distances (fig. 7c,f). According to fig. 6a, the Ni-Fe/Al_2O_3 catalyst is therefore structured as Ni-Fe nanoparticles distributed on the Al_2O_3 support. Due to the relatively low difference in mass between Ni, Fe and Al it can be difficult to distinguish between the nanoparticles from the oxide in term of mass-thickness contrast, in particular for the smallest particle sizes, even though an objective aperture was used to enhance the contrast.

Particle size distributions based on the TEM images of the Ni-Fe/Al_2O_3 samples with 5 – 23 wt.% metal loading are presented in fig. 8a. The particle size distributions show a main peak near 10 nm in diameter for all the catalysts, but with increasing metal loadings the tail to the large particle side of the main peak increases. The mean particle size is therefore increasing with the metal loading, and this can therefore partly explain the moderate increase in catalytic activity for increasing metal loadings, according to fig. 5. It should be noted that due to the relatively low mass-thickness contrast mentioned above, it cannot be excluded that a number of un-observed smaller particles (below ca. 5 nm) are present in the catalysts. To check for consistency, the mean particle size was

determined from the XRD patterns (fig. 3a) by using the Scherrer equation and the FWHM of the peaks corresponding to Ni-Fe. According the XRD data, the mean crystallite size is ca. 8 nm for the Ni-Fe/Al_2O_3 catalyst with 10% metal loading. This value is in reasonable agreement with the diameters obtained from TEM, when the measurement error and the fact that the nanoparticles may consist of smaller crystallites, is taken into account.

To relate the catalytic activity directly to the active surface area, fig. 8b presents the NH_3 conversion as a function of the metal surface area calculated from the particle size distributions and the metal loading by assuming a spherical particle-geometry. The conversion is presented for four different temperatures from test A and test B. These specific four environments (temperature and gas composition) represent intermediate conversion values i.e. values, not too close to 0% or 100% for most data points. According to fig. 8b, the NH_3 conversion scales only weakly with the active surface area.

To further investigate the relation between the catalytic activity and the particle sizes, the turnover frequencies of NH_3 (TOF) was calculated from the determined metal surface areas and assuming a surface atom density of $1.2 \cdot 10^{15}$ atoms/cm^2 which is a mean of the surface atom density for the [110], [111] and [100] lattice planes calculated from the Miller indices [25]. According to fig. 8c, the TOF is not constant, but increases significantly for decreasing particle sizes for all four temperatures and gas environments. Since the relative number of edge sites of supported metal particles decrease with the particle size, the trend observed in fig. 8c indicates a higher catalytic activity for NH_3 decomposition on edge sites than on terraces. This result is consistent with previously reported structure sensitivity for NH_3 decomposition with catalysts based on Ni [26,27] or K-promoted Fe [7] and with the well-established surface sensitivity for the NH_3 synthesis reaction [28,29]. For NH_3 synthesis, N_2 dissociation is the rate limiting step, and the rate of the dissociative adsorption of N_2 on Ru has been shown to be a least 9 orders of magnitude higher on steps than on terraces [30]. For the NH_3 decomposition reaction, the rate limiting step has been suggested to be the corresponding recombinative desorption of nitrogen [8], and the trend presented by fig. 8c is therefore likely related to a higher rate of recombinative desorption of nitrogen on step sites than on other types of surface sites.

3.5 Support materials

To investigate the possible influence of the oxide support on the NH_3 decomposition reaction for the Ni-Fe based catalysts, the catalytic activity of Ni-Fe/Al_2O_3 was compared to that of Ni-Fe/TiO_2, Ni-Fe/SiO_2, Ni-Fe/ZrO_2 and Ni-Fe/Mg-Al-spinel, all with an intended metal loading of 10 wt.% and 20 wt.% Ni in the active phase. Fig. 9 presents the NH_3 conversion for these catalysts as a function of reaction temperature for (a) test A and (b) test B. It should be noted, that the conversions from these tests of crushed pellets (fig. 9) are generally higher than observed for whole pellets of the same catalysts (fig. 2). This difference indicates that the reaction is limited by diffusion when whole catalyst pellets are used. Therefore, the catalytic activity can only be compared directly when the same pellet sizes are used where it can be assumed that the reaction is equally limited by diffusion.

For both tests, the catalytic activity of Ni-Fe/Mg-Al-spinel and Ni-Fe/Al_2O_3 are significantly higher than that of the other catalysts, and the figure suggests that overall catalytic activity can be improved by using Mg-Al-spinel instead of alumina as the support material. It is particularly interesting to observe that the NH_3 conversion is comparably to or even higher for these catalysts compared with the commercial Ru/Al_2O_3 catalyst in the H_2 rich gas environment at the highest temperatures. The Ni-Fe based catalysts therefore could be promising catalysts to replace Ru in systems where a high H_2 concentration in the end product is aimed at.

The catalytic activities of the other catalysts, Ni-Fe/TiO_2 in particular, are significantly lower than that of Ni-Fe/Al_2O_3 and Ni-Fe/Mg-Al-spinel. The effect of the support, as presented in fig. 9, is more pronounced than support effects reported for pure Ru, Ir or Ni and the order of decreasing activity is different [8,9,23].

Fig. 10 presents BET measurements of the surface areas of the oxides before and after reduction. According to these measurements, the surface areas of Al_2O_3 and Mg-Al-spinel are not influenced, the surface area of SiO_2 is decreased slightly, and the surface areas of ZrO_2 and TiO_2 in particular are significantly decreased by the thermal treatment. The BET measurements therefore indicate a rapid sintering of ZrO_2 and TiO_2 and possibly slow sintering of SiO_2 in H_2 at 800°C. The suggested sintering of TiO_2 in H_2 at 800ºC is consistent with the previously reported mobility of TiO_x species in H_2 already at 500ºC [31]. The loss of support surface area is likely also to result in a loss of the active surface area, and this effect could possibly explain the observed lower catalytic activity for the Ni-Fe catalysts supported on ZrO_2 and TiO_2 relative to those supported on Al_2O_3 or Mg-Al-spinel according to fig. 9. The surface area of SiO_2 is higher than that of all the other support oxides even though it appears to decrease slightly during the thermal treatment (fig. 10). The lower activity of Ni-Fe supported on SiO_2 compared to Al_2O_3 or Mg-Al-spinel, can therefore not be explained from the BET measurements.

To further investigate the structural differences between the Ni-Fe/oxide catalysts for the different support materials TEM and TEM-EDS was used for imaging and elemental analysis, respectively. Fig. 6b-e shows presents representative TEM images of (b) Ni-Fe/Mg-Al-spinel, (c) Ni-Fe/SiO_2, (d) Ni-Fe/ZrO_2 and (e) Ni-Fe/TiO_2 in comparison with the TEM image of Ni-Fe/Al_2O_3 (fig. 6a). The images of Ni-Fe/Mg-Al-spinel and Ni-Fe/SiO_2 are roughly similar to those of Ni-Fe/Al_2O_3, but small variations can qualitatively be observed in the structure of the support and in the Ni-Fe nanoparticle sizes (fig. 6a-c). A different structure is clearly observed for Ni-Fe/ZrO_2 (fig. 6d) where the irregular area must correspond to an agglomerate of larger oxide grains compared to the other support oxides (fig. 6a-d). This observation suggests a lower surface area of ZrO_2 compared to the other oxides in agreement with the BET measurements (fig. 10). Smaller nanoparticles cannot be distinguished from ZrO_2 in fig. 6d, which is not surprising considering the large mass of Zr relative to Ni and Fe. For this reason it is not possible to determine the physical structure of the Ni-Fe phase from the TEM images. As observed for Ni-Fe/Al_2O_3, Ni-Fe/Mg-Al-spinel and Ni-Fe/SiO_2, the structure of Ni-Fe/TiO_2 is characterized by large irregular features that can be attributed to TiO_2 in which smaller approximately circular areas are observed, which may be attributed to the Ni-Fe phase (fig. 6e). But the structure of Ni-Fe/TiO_2 also have significant differences from that of the

other catalysts: The TiO_2 consists of very large grains (note the longer scale bar for fig. 6e) indicating a low support surface area compared to all the other oxides, consistent with the BET measurements (fig. 10). The observed Ni-Fe nanoparticles are also significantly lager in this catalyst than in the other catalysts.

According to the TEM EDS results presented in fig. 11a, for all catalysts, except Ni-Fe/TiO_2, the metal loading is ca. 7% and the Ni concentration in the active phase is ca. 20%, close to the intended values of 10% and 20%, respectively. It should be noted that TEM EDS is only probing a small area of the samples and the results can therefore only be used as approximations. For the Ni-Fe/TiO_2 catalyst the metal loading is higher, and the Ni concentration lower, relative to the other samples. The higher metal loading could indicate a loss of TiO_2 mass, e.g. by removal of oxygen during the reduction H_2 at 800ºC. In fig. 11b, the oxygen concentration in the oxides, calculated based on the TEM EDS measurements, is presented for each catalyst together with the calculated stoichiometric value. Indeed, the TiO_2 support has been reduced according the TEM EDS measurements. This result agrees with previous studies, showing that the surface phase TiO_2 can be reduced into Ti_4O_7 at in H_2 at temperatures above 600ºC [31,32]. Also, the ZrO_2 support has apparently been reduced during the pretreatment according to fig. 11b. This could also have been expected, since reduction of ZrO_2 in H_2 already takes place at ca. 550ºC [33].

BET, TEM images and TEM EDS therefore consistently suggest that ZrO_2 and TiO_2 have been partly reduced and have sintered during the reduction process (fig. 6, fig. 10 and fig. 11).

Particle size distributions based on the TEM images of Ni-Fe/Al_2O_3, Ni-Fe/Mg-Al-spinel, Ni-Fe/SiO_2 and Ni-Fe/TiO_2 are presented in fig. 12. Since the Ni-Fe nanoparticle could not be distinguished in the TEM images of Ni-Fe/ZrO_2 a particles size distribution for this catalyst is not presented. In agreement with fig. 6 the Ni-Fe nanoparticle sizes vary significantly for the different oxides. It is interesting to notice that except for TiO_2, the Ni-Fe nanoparticle sizes (fig. 12) are not correlated with the support surface area (fig. 10). This could suggest a higher degree of sintering in the reducing environment for Ni-Fe nanoparticles on SiO_2 than on Mg-Al-spinel and Al_2O_3.

Interestingly, the order of increasing particle sizes for the catalysts; Ni-Fe/Mg-Al-spinel < Ni-Fe/Al_2O_3 < Ni-Fe/SiO_2 < Ni-Fe/TiO_2 is identical to the order of decreasing catalytic activity for these catalysts (fig. 9, fig. 12). This suggests that the variation in catalytic activity for the Ni-Fe nanoparticles on the different oxide support materials (fig. 9) can partly be explained by the differences in the total active surface area and by the structural effect discussed above. In a previous study of the decomposition of NH_3 with a Ru-based catalyst, the following order or decreasing activity was found: Ru/CNTs > Ru/MgO > Ru/TiO_2 ≈ Ru/Al_2O_3 ≈ Ru/ZrO_2 > Ru/AC [9] and these trends were partly explained by differences in surface area, conductivity and acidity. It has also been reported that Ni has a higher activity when supported on SiO_2 than when supported on Al_2O_3 [23]. The currently observed catalytic activities cannot be related directly to the support acidity or conductivity, and further studies are needed to deconvolute such support effects.

3.6 Preparation method

Since small Ni-Fe nanoparticle sizes are crucial for high NH_3 conversions (fig. 8c), methods for obtaining the smallest possible nanoparticles should be considered. Since the supported Ni-Fe nanoparticles are likely to sinter in H_2 at 800°C, an obvious route for lowering the mean particle size would be a milder reduction process at a lower temperature. In the present study, we focus on for example fuel cell applications where a high concentration of H_2 is needed and therefore relatively high reaction temperatures (700 - 800°C) are needed. For the current study it would therefore be interesting to find other methods for lowering the Ni-Fe particle sizes. One way of obtaining smaller Ni-Fe particle sizes could possibly be to synthesize the catalysts by coprecipitation of the metal salts for both the catalytically active phase and for the oxide support. By this method the Ni-Fe particles may be integrated within the larger network of Al_2O_3 which could help to lower the degree of sintering during the thermal treatments.

A Ni-Fe/Al_2O_3 catalyst with an intended metal loading of 10% and with a Ni concentration in the active phase of 20% was therefore prepared by this method, and the NH_3 conversions are presented in fig. 9a-b in comparison with the catalysts prepared by incipient wetness impregnation of different support types. The NH_3 conversion of the catalyst prepared with coprecipitation is comparable to that of the best catalyst prepared by impregnation, Ni-Fe/Mg-Al-spinel (fig. 9). According to TEM, the structure of the catalyst prepared by coprecipitation is roughly similar to that of the impregnated Ni-Fe/Al_2O_3 catalyst (fig. 6a,f), but the Ni-Fe nanoparticle sizes are generally lower (fig. 12). The assumption of a lower degree of sintering of the former catalyst may therefore be true. The Ni-Fe nanoparticle sizes for the catalyst prepared by coprecipitation are, however, larger relative to the Ni-Fe/Mg-Al-spinel catalyst. It should also be mentioned that a core-shell structure was observed for the Ni-Fe nanoparticles and that this structure was most pronounce for the catalyst prepared by coprecipitation. In fig. 7d, a bright shell is for example clearly observed surrounding the darker cores. The core-shell structure probably resulted from a surface oxidation when the catalysts are exposed to air after testing [34]. Only the core was measured when measuring the particles sizes, and the mean particle size is therefore probably slightly larger during the operation conditions than given by the ex situ measured values.

Supported Ni and Fe nanoparticles have been reported to initiate sintering in a reducing environment above their Tamman temperature of ca. 600°C [35]. Although alloying in some cases have been reported to increase the resistance towards sintering [36-37], it may therefore be expected that the presented Ni-Fe-based catalysts will suffer from deactivation via sintering for longer process times during realistic operation conditions. Significant deactivation was not observed when comparing a treatment in H_2 at 800°C for 1 and 6 hours (fig. 4), but significant deactivation cannot be ruled out during treatments in a mixture of NH_3 and H_2 for many hours or days. Further studies of catalyst deactivation are therefore needed before practical applications of the presented catalysts.

4 Conclusions

The developed Ni-Fe catalysts for NH_3 decomposition are based on relatively inexpensive and abundant materials compared to the noble metal-based catalysts needed to achieve a comparable catalytic activity. The catalyst could be a promising candidate to replace more expensive noble

metal-based catalysts for decompositions of NH_3 in systems where a high concentration of H_2 (corresponding to low concentrations of NH_3) is needed. It is found that small Ni-Fe nanoparticle sizes are crucial for an optimal overall NH_3 conversion, not only because a small mean particle size is correlated with a large active surface are, but also because of a structural effect favoring the smallest particles in terms of catalytic activity per active site. Al_2O_3 or Mg-Al-spinel is found to be the preferable support type, contrary to SiO_2, ZrO_2 and TiO_2 on which small Ni-Fe nanoparticles sizes are challenging to obtain under the reaction conditions partly due to sintering and reduction of the support oxide.

5 Acknowledgements

Center for Individual nanoparticle Functionality (CINF) is funded by the Danish national research Foundations. The authors would like to thank the EUROSTARS program for funding this research project, Dmitry E. Dorokin, DTU CASE and Irek Sharafutdinov, DTU CASE for assistance in the catalyst test lab and Christian D. Damsgaard, DTU CEN for assistance with the in situ XRD measurement.

6 References

[1] L. Schlapbach, A. Züttel, Nature 414 (2001) 353-358.

[2] A. Klerke, C.H. Christensen, J.K. Nørskov, T. Vegge, J. Mater. Chem. 2008, 18, 2304-2310.

[3] R. Metkemeijer, P. Achard, Int. J. Hydrogen Energy 19 (1994) 535-542.

[4] C.H. Christensen, R.Z. Sørensen, T. Johannessen, U.J. Quaade, K. Honkala, T.D. Elmøe, R. Køhler, J.K. Nørskov, J. Mater. Chem. 15 (2005) 4106-4108.

[5] A. Ozaki, K. Aida, in: J.R. Anderson, M. Boudart (Eds.), Catalyses Science and Technology, Springer-Verlag, Berlin Heidelberg New York, 1981, pp. 87-158.

[6] S. Murata, K.-I. Aika, J. Catal. 136 (1992) 110-117.

[7] A. Jedynak, Z. Kovalczyk, D. Szmigiel, W. Raróg, J. Zielinski, Appl. Catal. A-Gen 237 (2002) 223-226.

[8] S.-F. Yin, B.Q. Xu, X.P. Zhou, C.T. Au, Appl. Catal. A-Gen 277 (2004) 1-9.

[9] S.-F. Yin, Q.-H. Zhang, B.-Q. Xu, W.-X. Zhu, C.-F. Ng, C.-T. Au, J. Catal. 224 (2004) 384-396.

[10] S.J. Wang, S.-F. Yin, L. Li, B.-Q. Xu, C.-F. Ng, C.-T. Au, Appl. Catal. B-Environ 52 (2004) 287-299.

[11] D. Szmigiel, W. Raróg-Pilecka, E. Miskiewicz, Z. Kaszkur, Z. Kowalczyk, Appl. Catal. A-Gen 264 (2004) 59-63.

[12] J. Donald, C. Xu, H. Hashimoto, E. Byambajav, Y. Ohtsuka, Appl. Catal. A-Gen 375 (2010) 124-133.

[13] F. Schüth, R. Palkovits, R. Schögl, D.S. Su, Energy Environ. Sci. 5 (2012) 6278-6289.

[14] A. Logadottir, T.H. Rod, J.K. Nørskov, B. Hammer, S. Dahl, C.J.H. Jacobsen, J. Catal. 197 (2001) 229-231.

[15] A. Boisen, S. Dahl, J.K. Nørskov, C.H. Christensen, J. Catal. 230 (2005) 309-312.

[16] C.J.H. Jakobsen, S. Dahl, B.S. Clausen, S. Bahn, A. Logadottir, J.K. Nørskov, J. Am. Chem. Soc. 123 (2001) 8404-8405.

[17] US Patent Application 20020021995, publication year: 2003

[18] US Patent 5679313, publication year: 1997

[19] WO Patent 9840311, publication year: 1998

[20] WO Patent 2010/060736 A1, publication year: 2010

[21] D. Freedman, P.Z. Diaconis, Wahrscheinlichkeit 57 (1981) 453-476.

[22] T.V. Choudhary, C. Sivadinarayana, D.W. Goodman, Catal. Lett. 72 (2001) 197-201.

[23] T.V. Choudhary, D.W. Goodman, Catal. Today 77 (2002) 65–78.

[24] T.B. Massalski, H. Okamoto (Eds.), Binary Alloy Phase Diagrams, ASM International, Ohio, 1990.

[25] K.W. Kolasinski, Surface Science: Foundations of Catalysis and Nanoscience, 2ed, John Wiley & Sons, West Sussex, 2008

[26] J. Zhang, H. Xu, W. Li, Appl. Catal. A-Gen 296 (2005) 257-267.

[27] M. Grunze, M. Golze, R.K. Driscoll, P.A. Dowben, J. Vac. Sci. Technol. 18 (1981) 611-615.

[28] G.A. Somerjai, N. Materer, Top. Catal. 1 (1994) 215-231.

[29] S. Dahl, E. Törnqvist, C.J.H. Jacobsen, J. Catal. 198 (2001) 97-102.

[30] S. Dahl, A. Logadottir, R.C. Egeberg, J.H. Hansen, I. Chorkendorff, E. Törnqvist, J.K. Nørskov, Phys. Rev. Lett. 83 (1999) 1814-1817.

[31] M.A. Vannice, L.C. Hasselbring, B. Sen, J. Phys. Chem. 89 (1985) 2972-2973.

[32] S.J. Tauster, S.C. Fung, R.T.K. Baker, J.A. Horsley, Science 211 (1981) 1121-1125.

[33] D. Eder, R. Kramer, Phys. Chem. Chem. Phys. 4 (2002) 795–801.

[34] L.T. Kuhn, A. Bojesen, L. Timmermann, M.M. Nielsen, S. Mørup, J. Phys. Condens. Matter. 14 (2002) 13551-13567.

[35] R.T.K. Baker, J. Catal. 78 (1982) 473-476.

[36] M. Chen, L.D. Schmidt, J. Catal. 56 (1979) 198-218.

[37] J. Zhang, K. Sasaki, E. Sutter, R.R. Adzic, Science 315 (2007) 220-222.

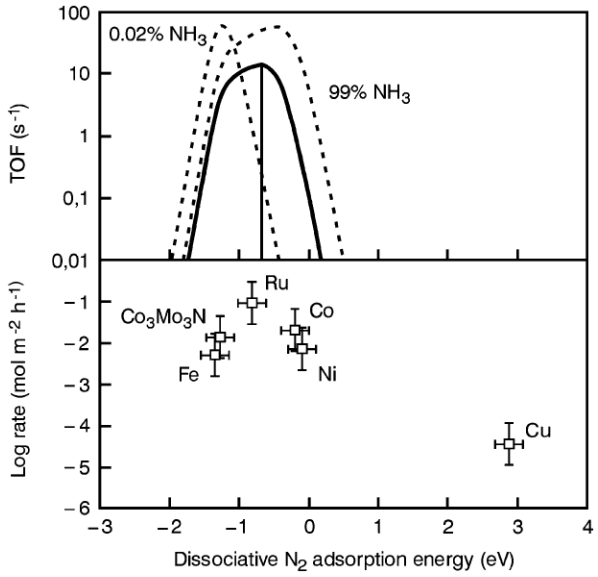

Fig. 1: (Top) Calculated turnover frequencies of ammonia synthesis/decomposition at 773 K, 1 bar, 3:1 H_2/N_2, and 0.02, 20 (solid line), and 99% NH_3 as a function of the reaction energy of dissociative N_2 adsorption. (Bottom) Experimental rates of ammonia decomposition over various catalysts at 773 K, 1 bar, 3:1 H_2/N_2, and 20% NH_3. Reprinted with permission from reference [15].

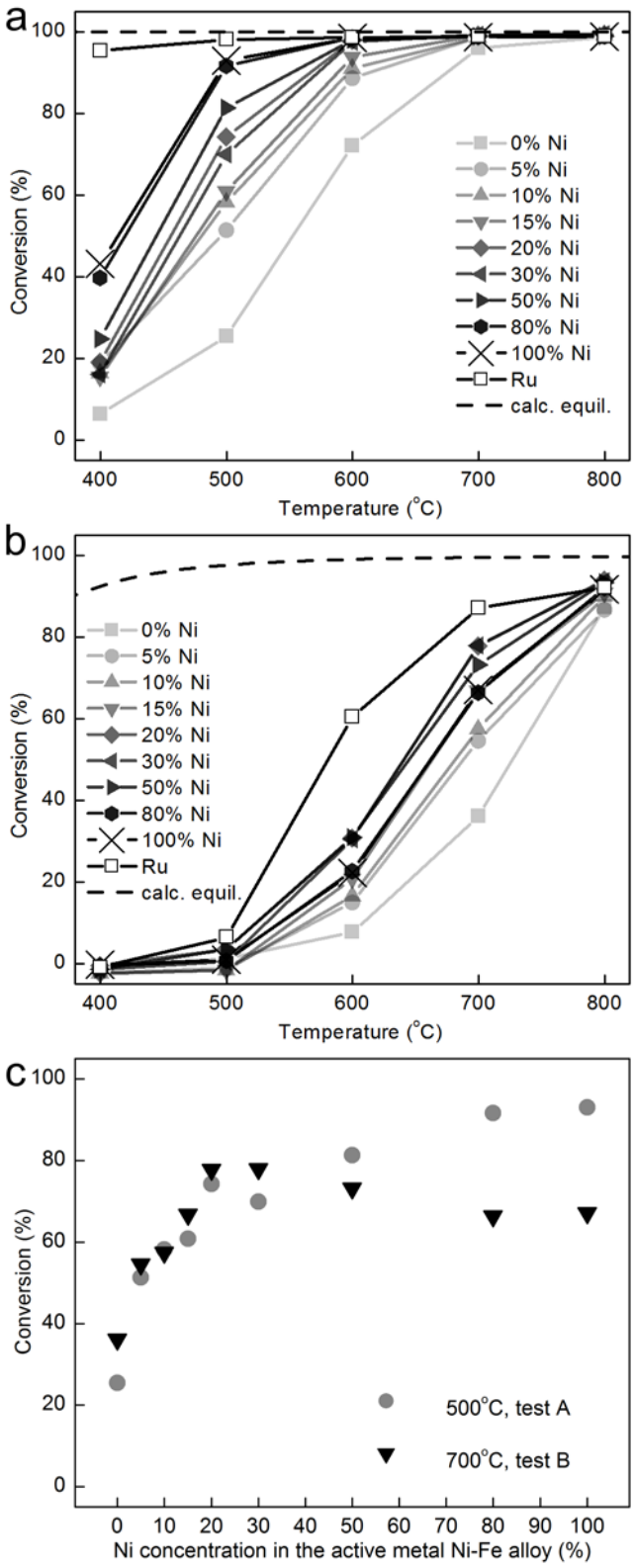

Fig. 2: The NH_3 conversion presented as a function of reaction temperature for (a) test A and (b) test B of a series of Ni-Fe/Al_2O_3 catalysts . The Ni concentrations of the active metal Ni-Fe alloys in the catalysts vary from 0 to 100 % as indicated in the fig., and the metal loading for all catalyst are 10 wt.%. For comparison, the calculated thermodynamic equilibrium and the conversion for a

commercial 2 wt.% Ru/Al_2O_3 (same type of Al_2O_3 pellets) catalyst is also presented. (c) The NH_3 conversion from (a-b) is presented as a function of Ni concentration to emphasize the effect of varying the Ni-Fe alloy composition. For simplicity, only the data for two test conditions are presented: test A 500°C (from a) and test B 700°C (from b). For all catalysts, the test is performed on whole catalyst pellets.

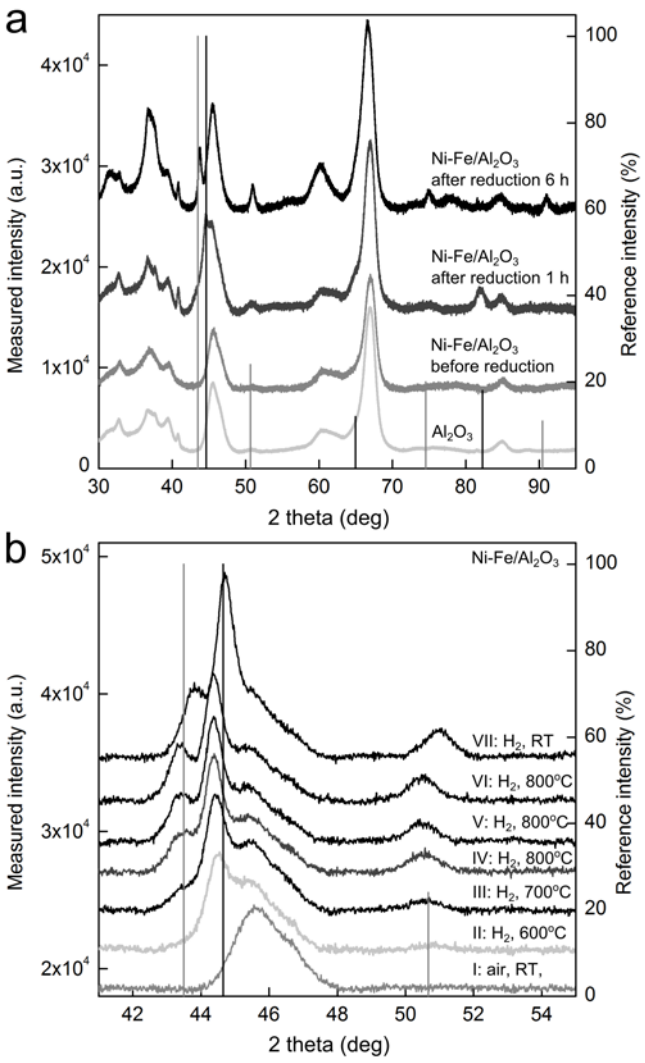

Fig. 3: (a-b) XRD patterns of a Ni-Fe/ Al_2O_3 catalyst with 20 wt% Ni in the active metal phase and 10 wt.% metal loading. (a) ex situ XRD before and after reduction in H_2 at 800°C for 1 h or 6 h as indicated in the figure. A patterns of the Al_2O_3 support is also presented for comparison. (b) in situ XRD where the patterns are recorded in the order indicated by roman letters and present a reduction process in H_2 as a function of time and temperature as indicated in the figure. (a-b) The vertical lines present the relative intensities from reference patterns of the Ni-Fe alloys; Kamacite (black) and Taenite (grey).

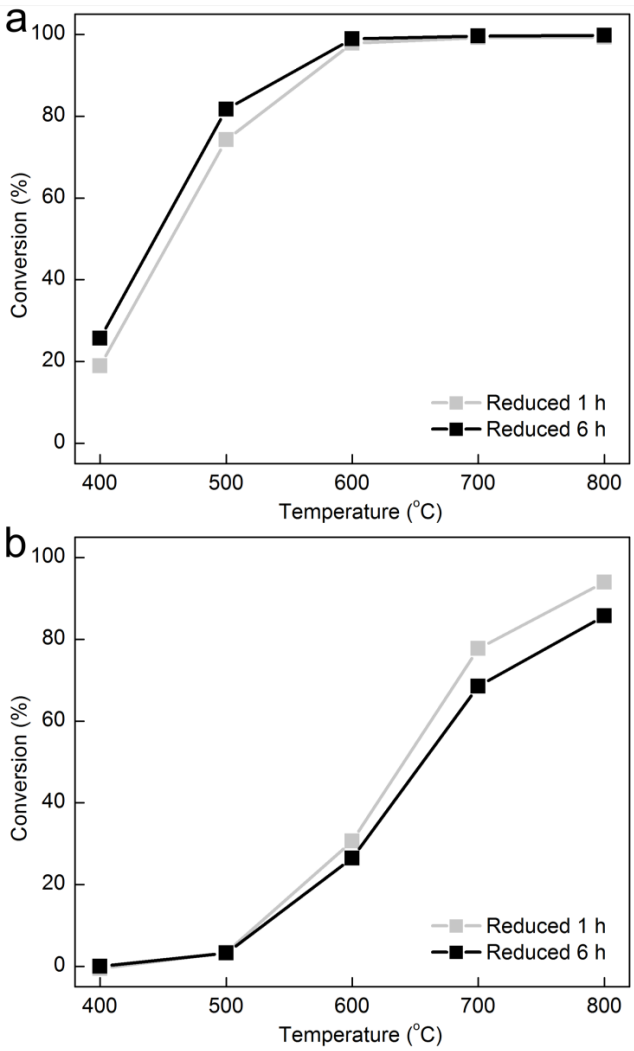

Fig. 4: The NH_3 conversion is presented as a function of reaction temperature for (a) test A and (b) test B of two Ni-Fe/Al_2O_3 catalysts. One of the catalyst was reduced for 1 h (grey) and the other was reduced for 6 h (black). The Ni concentrations of the active metal Ni-Fe alloys in the catalysts is 20%, and the metal loading is 10 wt.%. For both catalysts, the test is performed on whole catalyst pellets.

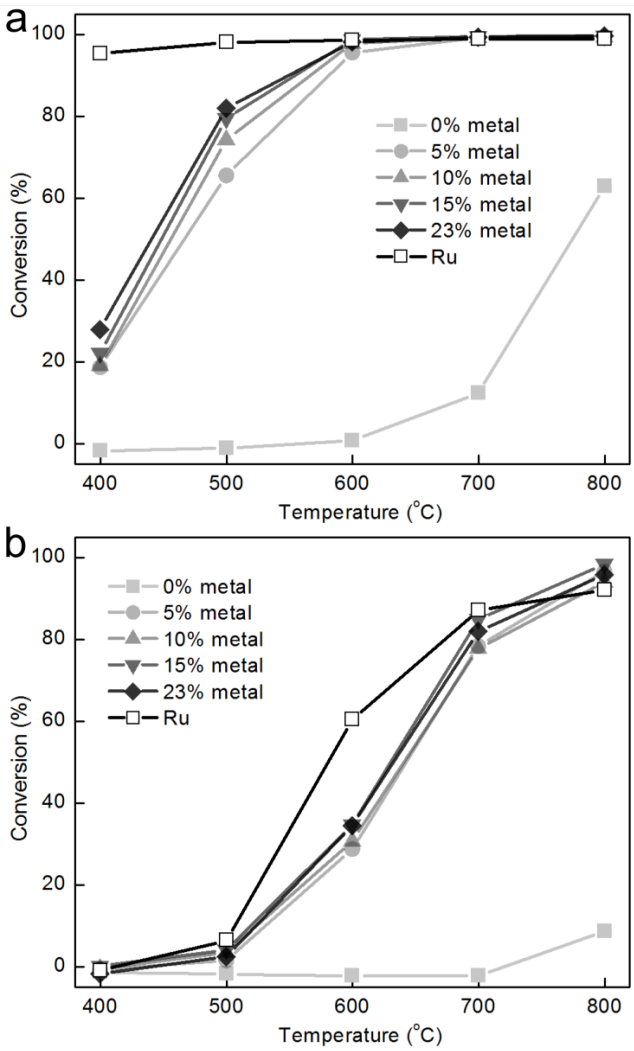

Fig. 5: The NH_3 conversion is presented as a function of reaction temperature for (a) test A and (b) test B of a series of Ni-Fe/Al_2O_3 catalysts. The Ni concentrations of the active metal Ni-Fe alloys in the catalysts was 20 wt.%, and the metal loading was varied from 0 - 23 wt.% as indicated in the figure. For comparison, the conversion for a commercial 2 wt.% Ru/Al_2O_3 (same type of Al_2O_3 pellets) catalyst is also presented. For all catalysts, the test is performed on whole catalyst pellets.

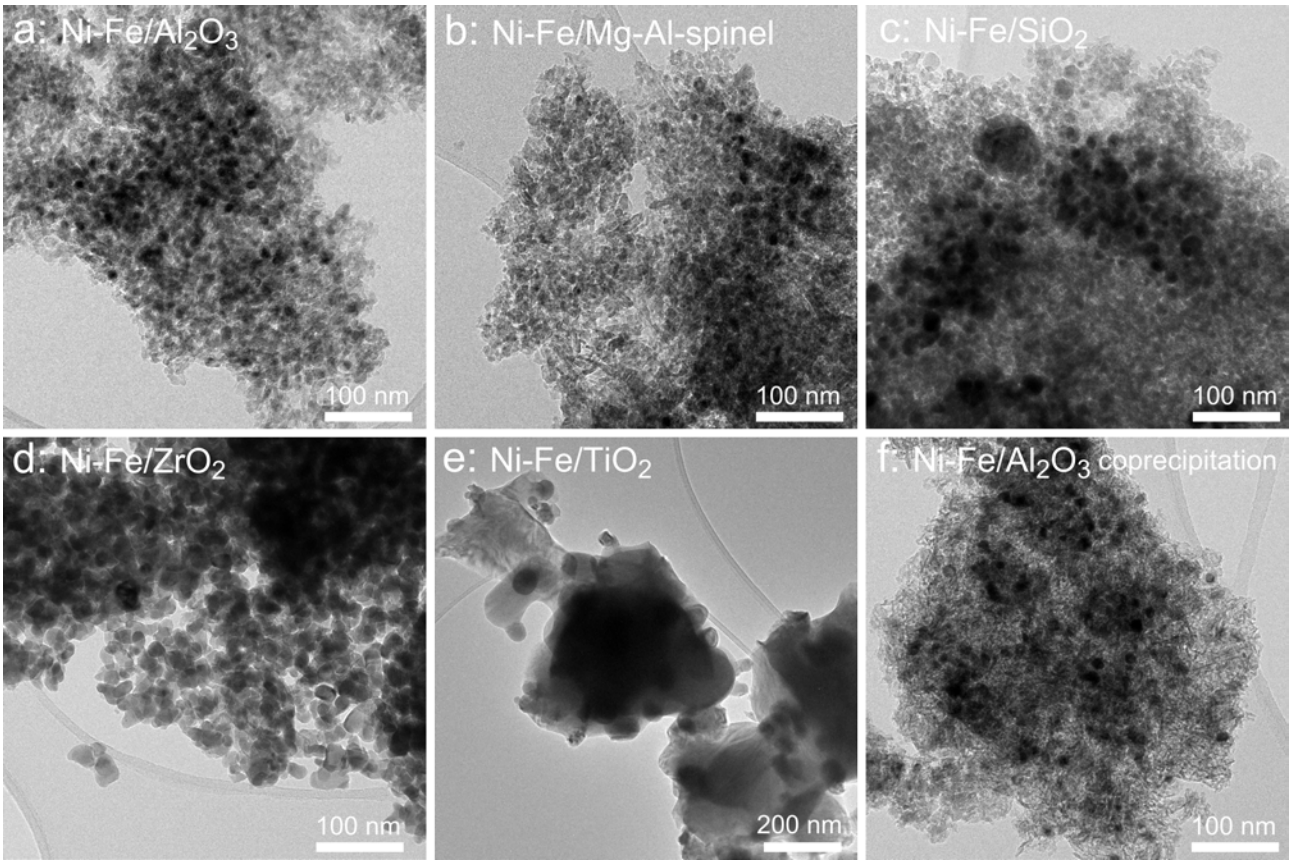

Fig. 6: TEM images of the (a) Ni-Fe/Al_2O_3, (b) Ni-Fe/Mg-Al-spinel, (c) Ni-Fe/SiO_2, (d) Ni-Fe/ZrO_2, (e) Ni-Fe/TiO_2 catalysts prepared by incipient wetness impregnation. (f) TEM image of the Ni-Fe/Al_2O_3 catalyst prepared by coprecipitation. The scales are identical for all images, except for (e) as indicated by the scale bars.

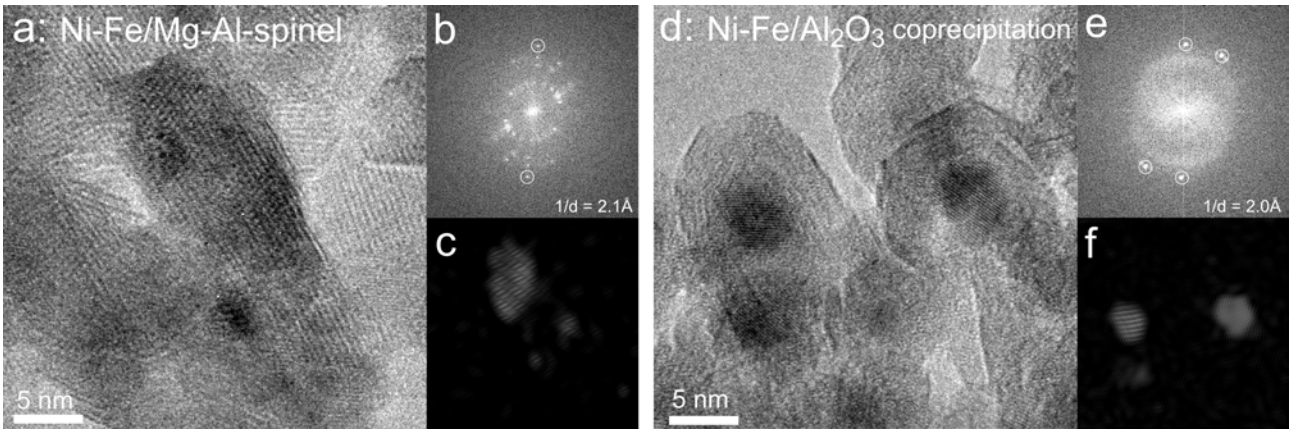

Fig. 7: HRTEM images of the (a) Ni-Fe/Mg-Al-spinel and (d) Ni-Fe/Al_2O_3 catalyst prepared by coprecipitation. In the corresponding Fourier transforms (b,e), spots appear which corresponds to a lattice distance of 2.0 Å and 2.1 Å (indicated with circles). The additional longer lattice spacing result from the support material. (c,f) Inverse Fourier transforms of the masked areas indicated by circles in (b,e) show which areas in the original TEM images the lattice spacing of 2.0 – 2.1 Å adheres from.

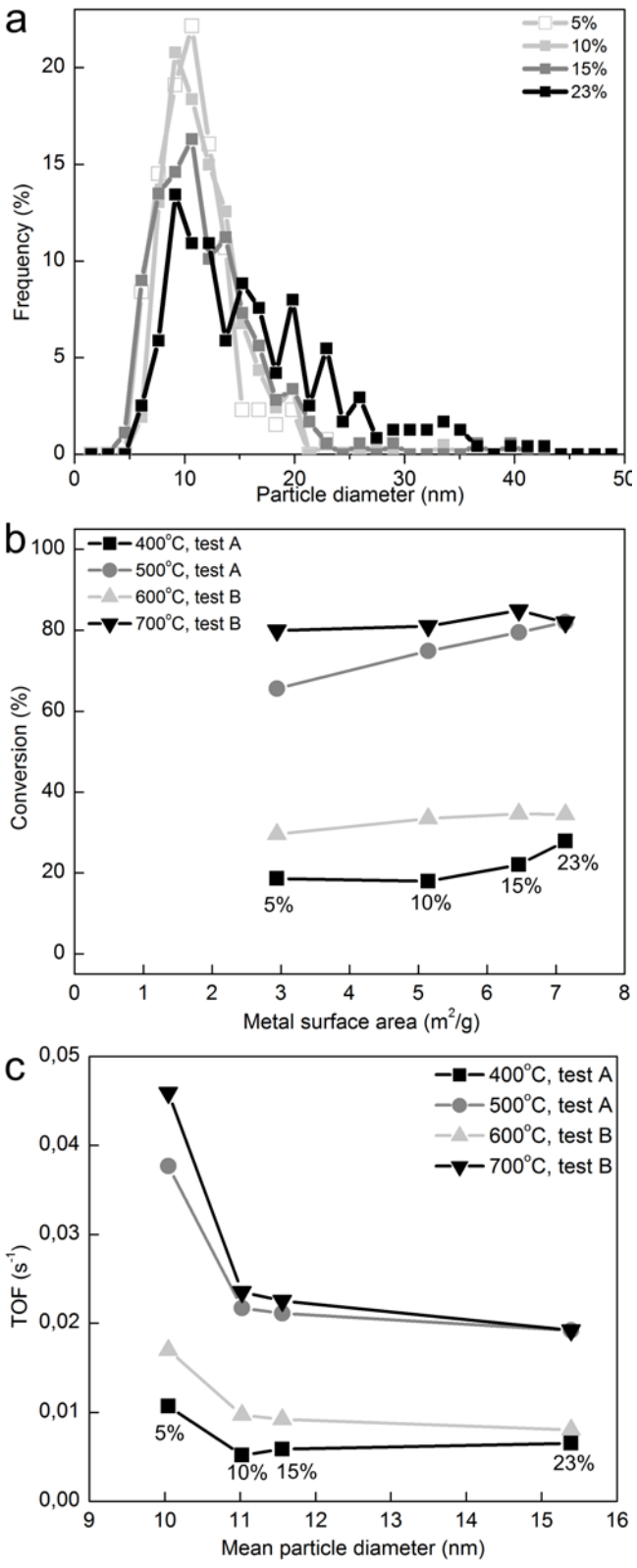

Fig. 8: (a) Particle size distributions based on TEM images of Ni-Fe/Al_2O_3, with 5%, 10%, 15% and 23% metal loading. Note that the histograms in the figure are represented by lines + symbols instead of columns. The bin size was optimized for the data of the sample with 10% metal loading, and this bin size was used for all histograms. The number of particles in each histogram is 131

(5%), 207 (10%), 178 (15%) and 238 (23%). (b) The NH_3 conversions from fig. 5 presented as a function of the calculated metal surface area for each of the catalysts. (c) The TOF of NH_3 is presented as a function of the mean particle size for each catalyst. The calculated metal surface areas and the TOFs are based on the metal loading and the particle size distributions for each catalyst.

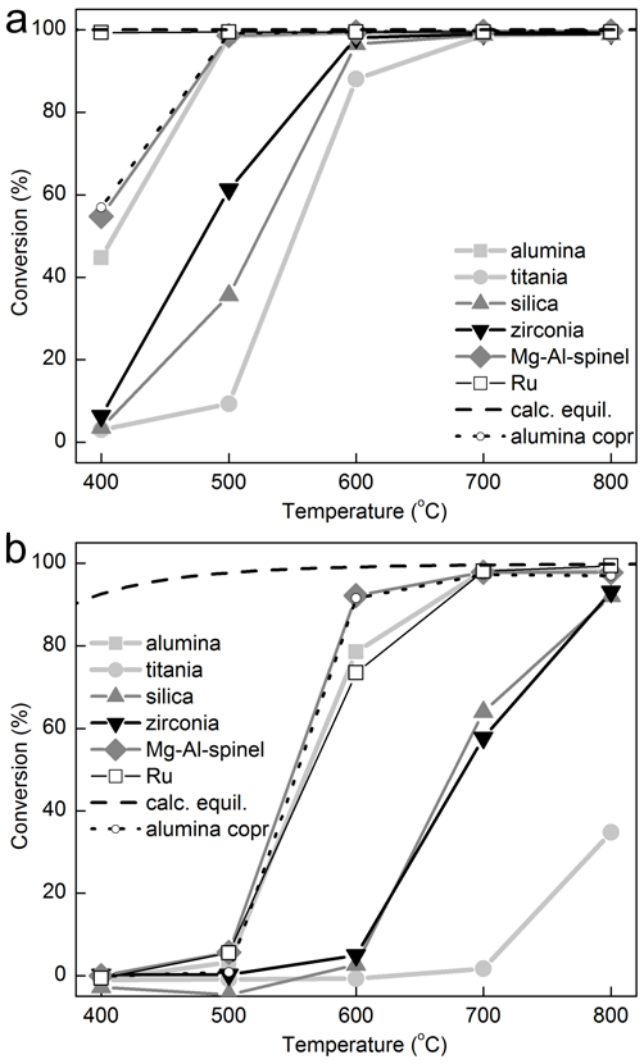

Fig. 9: The NH_3 conversion is presented as a function of reaction temperature for (a) test A and (b) test B of a series of catalysts with Ni-Fe alloyed nanoparticles supported on Al_2O_3, TiO_2, SiO_2, ZrO_2 or Mg-Al-spinel. The conversion of a Ni-Fe/Al_2O_3 catalyst prepared by coprecipitation is also presented. For comparison, the calculated thermodynamic equilibrium and the conversion of a commercial 2 wt.% Ru/Al_2O_3 (same type of Al_2O_3 pellets) catalyst is also presented. To exclude a possible influence of variations in support pellet sizes and shapes, all catalyst pellets were crushed down to gains of an identical size range (ca. 200 – 400 µm).

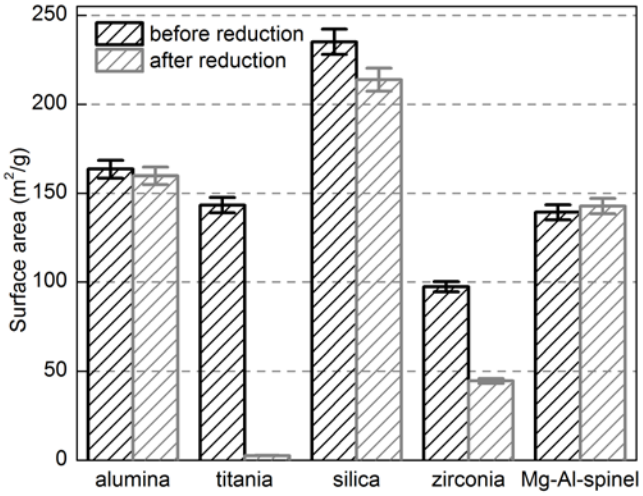

Fig. 10: BET surface areas of the support materials Al_2O_3, Mg-Al-spinel, SiO_2, TiO_2 and ZrO_2 before and after reduction in H_2 for 5 h at 800°C. The error bars indicate the estimated measuring errors.

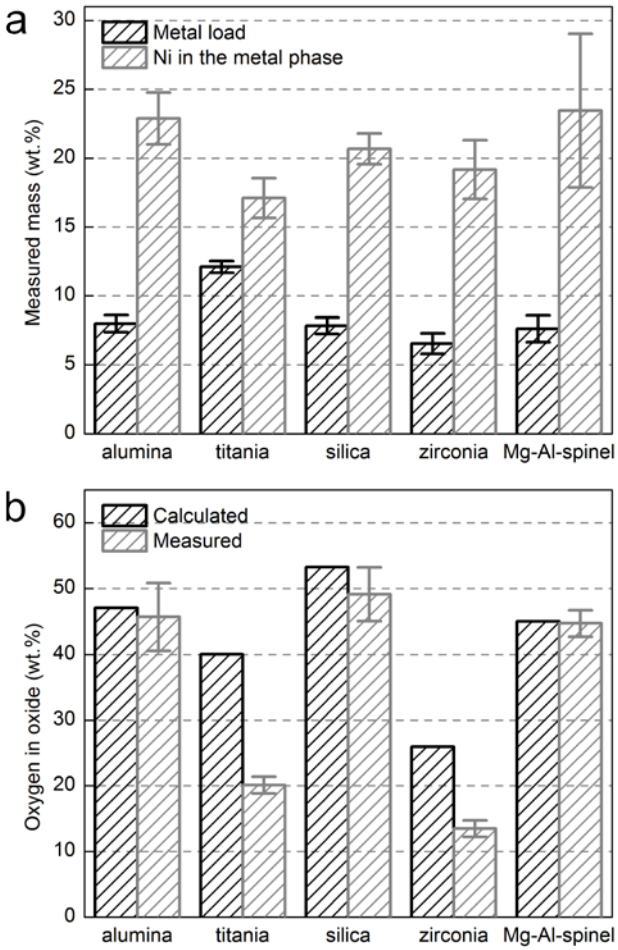

Fig. 11: (a) The metal loading and Ni percent in the active phase measured by TEM EDS for Ni-Fe/Al_2O_3, Ni-Fe/TiO_2, Ni-Fe/SiO_2, Ni-Fe/ZrO_2 or Ni-Fe/Mg-Al-spinel. (b) The oxygen content in

the support materials, either calculated or measured by TEM EDS, is presented for the Ni-Fe/oxide catalysts. All TEM EDS measurements represent averaged results from three different sample areas of ca. 2 μm^2. The error bars indicate the standard deviation.

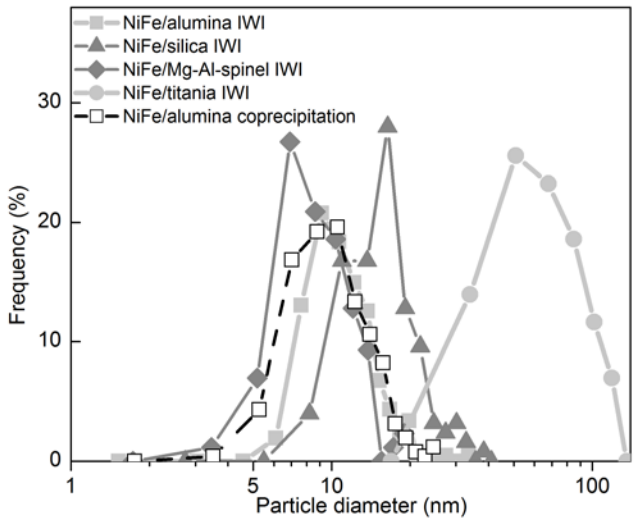

Fig. 12: Particle size distributions based on TEM images of Ni-Fe/Al_2O_3, Ni-Fe/SiO_2, Ni-Fe/Mg-Al-spinel and Ni-Fe/TiO_2 prepared by incipient wetness impregnation (IWI) and of Ni-Fe/Al_2O_3 prepared by coprecipitation. Note that the histograms in the figure are represented by lines + symbols instead of columns. Due to the large variation in particles sizes, the bin size has been optimized for each separate histogram. The areas of the distributions are therefore not directly comparable. The number of particles in each histogram is 207 (Ni-Fe/Al_2O_3), 125 (Ni-Fe/SiO_2), 86 (Ni-Fe/Mg-Al-spinel), 43 (Ni-Fe/TiO_2) and 255 (Ni-Fe/Al_2O_3 coprecipitation).